AEROACOUSTICS

Beamforming in Non-ideal Acoustic Environments

(Grid Adaptation for L_1 Norm Generalized Inverse Beamforming)

Péter Tóth

Environmental and Applied Fluid Mechanics Department, von Karman Institute for Fluid Dynamics, Belgium, tothp@vki.ac.be
Fluid Mechanics Department of Budapest University of Technology and Economics, toth@ara.bme.hu

Supervisor: Christophe Schram

Associate Professor, Environmental and Applied Fluid Dynamics Department, Aeronautics and Aerospace Department, von Karman Institute for Fluid Dynamics, Belgium, schram@vki.ac.be

University Supervisor: Máté Márton Lohász

Assistant Professor, Department of Fluid Mechanics, Budapest University of Technology and Economics, Hungary, lohasz@ara.bme.hu

Abstract

This paper presents some advancement of the acoustics beamforming technique developed in the VKI. The development is focusing on the L_1 norm generalized inverse beamforming methodology. The algorithms are improved and the present study introduces an adaptive methodology to refine the source grid. The refinement gives a non-uniform, unstructured source plane grid. The method helps to achieve similar results compared to the uniform grid solution with reduced number of grid points. This is useful when the searching zone and the grid is relatively large compared to the extent of the true sources. With this method the required computational resources for the inversion procedure can be decreased. Results are promising, but still improvement of the adaptive refinement algorithm is advisable. The performance of the algorithm is presented in this paper on a numerical test case for the generalized inverse beamforming algorithm.

Keywords: acoustics, generalized inverse, beamforming, adaptive grid, condition number

1. Introduction

There is an increasing desire for acoustic noise reduction of machines, those principles of fluid mechanics nature. Along with the numerical aeroacoustic advancements of understanding the principles of aerodynamic noise sources the need for experimental testing is increased to quantify complex sources or provide validation database.

The aim of this PhD project is to develop quantitative acoustics measurement configuration for aeroacoustic source localization in non-ideal acoustics environments. In several cases it is desirable to preform aeroacoustic measurements in non-anechoic environments, such as aerodynamic wind tunnels or in situ industrial measurements. The beamforming technique would extend the use of advanced aeroacoustic testing in a cost efficient way in such environments. The beamforming method was first used in radio astronomy and radar technology to obtain a directionally sensitive antenna for the detection of the incoming signal direction [1]. The principle of this technique is to utilize the signal of several microphones in such a way that the directional sensitivity of device is adjustable. This is usually achieved with digital signal processing techniques on the simultaneously acquired data of the microphones. The acoustics field can be scanned point by point in order to find the unknown source positions by 'steering' the array sensitive 'spot' (main lobe) into different spatial directions, at a given frequency. The result is the so called the beamforming map, shows the source amplitude distribution in the spatial region that have been scanned. Today's this technique is widely used in different configuration for acoustics source identification. Many application dependent microphone arrangement exist, using advanced data processing algorithms, in order

to obtain high resolution and clean source maps [2]. One of the method is using the mathematical concept of generalized inverse of matrices [3]. This is the technique used in the VKI beamforming project.

After the description of the motivation of the study, first the theoretical background of the used generalized inverse method will be presented in the first section. This is followed by a description of the grid adaptation technique and the used numerical source model. Then the adapted grid results will be shown compared to a conventional uniform grid. This is followed by the discussion of the results. Finally the study is concluded in the last section.

1.1. The motivation

The previous investigations in the VKI of the generalized inverse beamforming (GIBF) technique has been showed that the method is sensitive to the source modeling error introduced by a source grid that is not includes all the significant sources of the measurement. This is often a situation when uniform source grid is used and the measurement contains disturbing sources far from the investigated model. This is a typical situation of a measurement in non-ideal acoustic environment. These errors decrease the robustness of the method. The uniform grid is usually extended only with a small amount beyond the expected location of the sources in order to reduce the computation resources and in this way this type if grid is not suitable for such measurement cases.

The current study gives an attempt to solve the problem by automatically adjust the model source grid in order to place many grid points close to the approximate location of the sources and remove the model sources where no source is expected. The approximate location of the sources is detected by the first iteration on a uniform coarse grid that can be chosen to include not only the investigated sources but other disturbing sources as well. The adaptation of the grid later gives sufficient source resolution for the final iterations.

2. Theory

Many different beam-forming methods have been developed in the past few years for aeroacoustic applications [2]. In this section the generalized inverse beamforming method is introduced based on the formulation of [3] with iteratively reweighed least squares (IRLS) method for the solution of the L_1 norm problem.

2.1. The microphone array data model

The microphone array data represents the sound field generated by physical sound sources. These sources are modeled with an appropriate source model and then this model problem is solved to retrieve the unknown model source amplitudes those are supposed to give a good estimation of the true physical sources. In this paper monopole representation of the sound sources is assumed. The transfer matrix involves each model source and each microphone can be written as:

$$V_{k,l} = \frac{e^{-ik|\mathbf{r}(\mathbf{y}_k^m, \mathbf{y}_l^s)|}}{4\pi|\mathbf{r}(\mathbf{y}_k^m, \mathbf{y}_l^s)|} \tag{1}$$

where the transfer matrix $\mathbf{V}$ is called the array manifold matrix in beamforming terminology. The distance between the microphone position $\mathbf{y}_k^m$, $k = 1..N_m$, and source position $\mathbf{y}_l^s$, $l = 1..N_s$ is $r = \mathbf{y}_k^m - \mathbf{y}_l^s$. The wave number is $k = c/\omega$ at a given circular frequency ω. The number of microphones and model sources denoted by N_m and N_s respectively.

The model sources can be represented by their cross correlation matrix $\mathbf{C_{ss}}$ of size $N_s \times N_s$ formed by the unknown complex source amplitudes $\mathbf{s}$. The source cross spectrum matrix is diagonal if the model sources are perfectly uncorrelated (they are incoherent) giving a full rank matrix. The matrix is singular with the rank of one, if the model sources are perfectly correlated (coherent sources). Finally, in case of partly correlated model sources the matrix has a full rank, with non-zero off diagonal elements.

During the measurement, the microphone array cross spectrum matrix $\mathbf{C_{xx}}$ can be computed from the measurement time data with the help of fast Fourier transformation. The elements of $\mathbf{C_{xx}}$ represents the amplitude and phase correlation between the acoustics signal sampled at different spatial points. The rank of the array cross spectrum matrix indicates the number of incoherent sources. The array cross spectrum matrix $\mathbf{C_{xx}}$ can be represented by its eigendecomposition since it is Hermitian.

$$\mathbf{C_{xx}} = \mathbf{U\Lambda U}^\dagger \tag{2}$$

Introducing the previous source reconstruction idea that the model sources with proper amplitude distribution can describe measured cross spectrum the following relation can be written:

$$\mathbf{U\Lambda U}^\dagger = \mathbf{V C_{ss} V}^\dagger \tag{3}$$

This equation is the basis of the GIBF formulation.

2.2. Generalized Inverse Beamforming algorithm

The GIBF algorithms are based on the inversion of the wave propagation problem relating the assumed possible source distribution and the measured acoustic field. The idea of the reconstruction is to treat one coherent source distribution at a time, meaning that a microphone array cross spectrum matrix $\mathbf{C_{xx}}$ can be constructed from the summation of $\mathbf{C^n_{xx}}$ for each eigenvalue λ_n of $\mathbf{C_{xx}}$, where $n = 1..N$. The problem is solved for the desired number of eigenvalues and the final source map is the squared sum of the resulting reconstructed source maps for each n. The problem of Eqn. 3 can be simplified with this idea as follows:

$$\mathbf{u}^n \sqrt{\lambda_n} = \mathbf{V}\mathbf{s}^n \tag{4}$$

Introducing the notation $\mathbf{b}^n = \mathbf{u}^n \sqrt{\lambda_n}$ for the eigenmode n the following inverse problem has to be solved to retrieve coherent source amplitudes $\mathbf{s}^n$:

$$\mathbf{s}^n = \mathbf{V}^{-1}\mathbf{b}^n \tag{5}$$

In order to retrieve the source amplitudes generalized inverse method has to be used, because of the propagation model can contain more sources than microphones or vice verse, therefore the coefficient matrix of the problem is non-square.

Non-square coefficient matrices represent underdetermined problems when the number of unknowns is larger than the number of available observations $N_s > N_m$. Overdetermined system is also possible when the number of unknowns is less than the number of observations $N_s < N_m$. The non square matrices arising in the beamforming problems are usually underdetermined since the number of measurement points are limited by the applied hardware (the number of microphones and acquisition channels) and the number of unknown model source amplitudes are user determined by taking into considerations the resolution of the algorithm (that depends on the frequency of interest and the microphone array size) and the scanning zone size.

2.3. Regularized solution methodology

If the problem is underdetermined a robust solution of Eqn. 5 can be obtained by imposing additional a priori information on the sources. Certain order of smoothness of the solution can be such an additional information. In the simplest case a constraint giving priority to the source distributions with smaller norm can be constructed. In order to allow this side constrain to have an effect on the solution, the residual of the solution in some p norm $R_p = \|\mathbf{V}\mathbf{s}^n - \mathbf{b}^n\|_p$ is allowed to be higher than zero. These requirements can be formulated as a minimization of the following cost function.

$$J_p = \epsilon\|\mathbf{s}^n\|_p + \|\mathbf{V}\mathbf{s}^n - \mathbf{b}^n\|_p \tag{6}$$

The solution of the inverse problem formulated as a minimization problem helps to overcome on the problem of the often badly conditioned $\mathbf{V}$. The cost function of Eqn. 6 with $p = 2$ represents the original Tikhonov regularization problem where the regularization parameter is ϵ. The regularization parameter can be considered here as a user definable parameter controlling the balance between the solution norm and the residual norm R_p. If $\epsilon = 0$ the residual norm is minimized leading to the unregularized solution. This can give meaning full result in numerical test cases when the condition number of the array manifold matrix $\mathbf{V}$ is small and there is no measurement error present in $\mathbf{b}^n$. When $\epsilon = \infty$ the effect of the constraint vanishes and only the solution norm is minimized. This would essentially lead to the $\mathbf{s} \equiv 0$ solution. Excessive regularization also decrease the resolution of the source maps, due to suppressing the effect of the smallest singular values of $\mathbf{V}$ [4] . Knowing that the small or zero regularization gives non-physical results, in real measurement cases the amount of the applied regularization should be carefully adjusted to the investigated case otherwise quantitative beamforming or desired resolution is not possible. In order to choose an optimal regularization parameter the L-curve analysis is used in this study, by defining the optimum at the corner of the curve [5]. This is automatically detected by the algorithm in the present L_p norm implementation.

The solution of the minimization of the cost function Eqn. 6 with a given ϵ and $p = 2$ can be written as:

$$\mathbf{s}^n = \mathbf{V}^\dagger(\mathbf{V}\mathbf{V}^\dagger + \epsilon\mathbf{I})^{-1}\mathbf{b}^n \tag{7}$$

The resolution of this method is only slightly better than the least squares beamformer, and as it is proposed by Suzuki [6; 3] the issue can be addressed by replacing the L_2 norm with L_1 norm in the cost function Eqn.:6 (means $p = 1$)

This cost function prevents the spreading of the amplitudes between grid points close to each other. Contrary to the $p = 2$ case when direct solution is exist with Eqn. 7 the minimization problem of the cost function Eqn.: 6 with ($p \neq 2$) can be solved only with iterative procedures. One solution, that is proposed

by [3], is to use the iteratively reweighed least squares approach to obtain a solution.

$$\mathbf{s}^n_{q+1} = \mathbf{W}_q \mathbf{V}^\dagger (\mathbf{V}\mathbf{W}_q\mathbf{V}^\dagger + \epsilon \mathbf{I})^{-1}\mathbf{b}^n \qquad (8)$$

Here $\mathbf{W}_q = \mathrm{diag}(|\mathbf{s}^n_q|^{2-p})$ is a weighting diagonal matrix, and the iteration counter is q. The iteration is stopped when the solution norm begin to increase, or the maximum number of iteration is reached, that is $q_{max} = 15$ in this study.

During this iteration procedure the number of the unknown model sources can be decreased by removing the smallest amplitude sources at each iteration. This is increasing the speed of the iteration and can also increase the final resolution of the algorithm. However it is complicating the stopping criteria of the algorithm since small level sources can be removed by the inappropriate stopping criterion. This procedure is proposed to use by [3]. In this paper an alternative solution methodology is proposed by using an adaptive grid technique to reduce the number of points therefore speed up the iteration and allow the proper resolution of every sources on the source map. It is worth to note that the problems presented here always falls into the category of the underdetermined system of equation.

2.4. Adaptive re-meshing of the model source domain

For the adaptive modification of the model source positions an unstructured grid is created with the help of the algorithm presented in [7]. The meshing algorithm takes the geometry and a distance function as an input and it is initialized with a uniform grid point distribution. This initial grid point distribution is defined by the user as well as the boundaries of the 2D domain where the source model have to be imposed. The distance function is prescribed by the result of an initial GIBF calculation on the user defined uniformly meshed domain. In the present case this involves only one iteratively reweighed least squares iterations ($q = 1$ in Eqn. 8). The resulted source map is smoothed with a moving average filter in order to have a smooth size control function and it is used with the help of a linear interpolation function to obtain the relative distances in the location of every unstructured grid points for the meshing algorithm.

The peaks on this map prescribes where the mesh should be fine and the valleys where it can be coarse. In real situations when the aeroacoustic source nature is of broadband type, this grid can be used to calculate source amplitudes for the close spectral lines also and therefore it is not needed to be recomputed often.

3. Application on a numerical test

In this section the application of the presented adaptive model source grid generation and GIBF algorithm is presented on a numerical test.

3.1. The model of the true sources with added noise

The used test case consist of two monopoles placed at x, y coordinates $[-2\lambda, -2\lambda]$, and $[2\lambda, 2\lambda]$ respectively. The wavelength is denoted by λ. The source plane is placed 11.66λ away from the plane of the microphone array (corresponds to 1m at $f = 4000$Hz with the defined sound speed). Both monopole source has an amplitude of 1 kg/s^2. The used microphone array layout is a multi-arm spiral layout of 32 microphone positions, depicted in Fig. 1. The origin of the reference coordinate system is defined in the center of the array as it is shown in the picture.

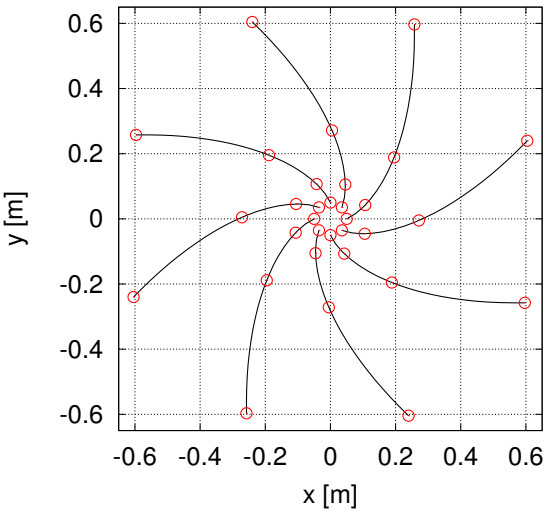

Figure 1: Optimized multi-arm spiral array geometry

In the presented test case the microphone array cross spectrum matrix $\mathbf{C_{xx}}$ is directly generated from the known position, frequency and amplitude of the imposed sources. In order to simulate realistic cross spectrum matrix additional noise is generated and introduced to this cross spectrum matrix. The sources are considered to be coherent.

3.1.1. Random noise cross spectrum model

The cross spectrum matrix is a positive semi definite Hermitian matrix. By introducing additional noise to simulate the real measurement scenario these

properties has to be respected. The array cross correlation is a transformation of the source cross correlation matrix with the array manifold matrix that is written for the true source locations. Since Eqn. 2 holds, each orthogonal eigenmode can be treated separately and their cross spectrum can be formed by the signal vectors $\mathbf{x}_s^n$.

$$\mathbf{C_{xx}} = \sum_{n=1}^{N_m} \mathbf{C}_{\mathbf{xx}}^n = \sum_{n=1}^{N_m} \frac{1}{K} \sum_{m=1}^{K} \mathbf{x}_s^{n,m} \mathbf{x}_s^{n,m\dagger} \tag{9}$$

Averaging process is taken place for K samples of the microphones signal vector (length N_m) can be written:

$$\mathbf{x}_s^n = \mathbf{V}\mathbf{s}^n + \mathbf{x}_{noise}^n \tag{10}$$

where $\mathbf{x}_{noise}^n$ is the additive noise formed by introducing a signal with random phase and constant amplitude as a fraction of the monopole source amplitude computed for the array center.

$$\mathbf{x}_{noise}^n = \beta \frac{\|\mathbf{s}^n\|}{4\pi L} e^{i2\pi\mathbf{w}} \tag{11}$$

where $\mathbf{w} \in U(0,1)$ is a vector of N_m elements from a uniform random distribution $U(0,1)$. The L is the array source distance (L = 1m in the study), $\mathbf{s}^n$ is the imposed source amplitude vector and β is a user defined parameter controlling the level of the introduced noise. The number of averages K also has an effect on the generated cross spectrum. As the number of averages increase the noise in the cross spectrum decrease while the auto spectra in the diagonal still contains the averaged level of noise. In this way cross spectrum matrix with similar white noise representation as of the real measurement scenarios can be build. The present test case $\beta = 0.05$ and $K = 60$.

4. Results

The normalized ordered eigenmodes of the noisy microphone array cross spectrum matrix is illustrated in Fig. 2. It can be seen that all the eigenmodes are non-zero due to the added random noise, but the first one has a significantly larger value than the others. This is the expected coherent mode, corresponds to the defined sources and the associated noise in that mode. In the reconstruction of the sources therefore only this eigenmode desired to be considered.

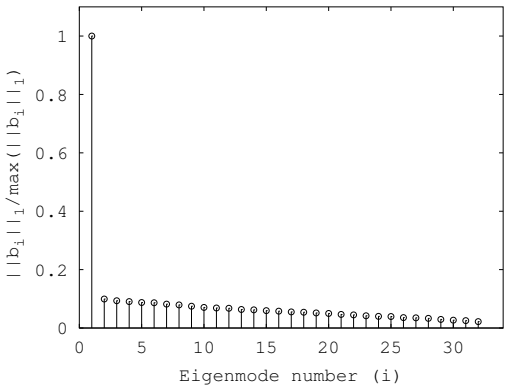

Figure 2: The normalized ordered eigenmodes for the test case

First the reconstruction is presented on a uniform grid without refinement. The grid size is chosen to be 6λ along which 101 grid points are placed in each directions. The reconstructed source map is presented in Fig. 3. Both sources are well retrieved. The source map spot size is about 0.3λ computed for the spot half width. The level of the spurious sources is small. The integrated source amplitude is approximately 0.5[kg/s^2] computed for the half width spot. In previous studies linear dependence of the source amplitude of the size parameters of integration region have been found, therefore the half width integrated value (size parameter 0.5) should correspond to approximately of the half of the true source amplitude. One should not forget that the added noise can cause some additional uncertainty. In the light of these considerations the reconstructed amplitude corresponds well to the true source amplitude as well as the position of the sources.

The reconstructed source field of the same microphone array cross spectrum matrix can be seen in Fig. 4 for the adapted grid. The distance function for the adaptive mesh generator was produced with one GIBF iteration on a 51×51 grid and the resulted source map is smoothed with a 19 point moving average filter. The final number of grid points is about 2930 in this adapted grid, and the model source distribution is plotted in Fig. 5. The model sources are strongly clustered around the true sources, while in the other regions of the source map few points are placed. The grid adaptation algorithm is used 20 retriangulations in order to obtain the present distribution of the points. The initial uniform distribution of the grid points for the grid generation algorithm is chosen in order to have approximately the same model source

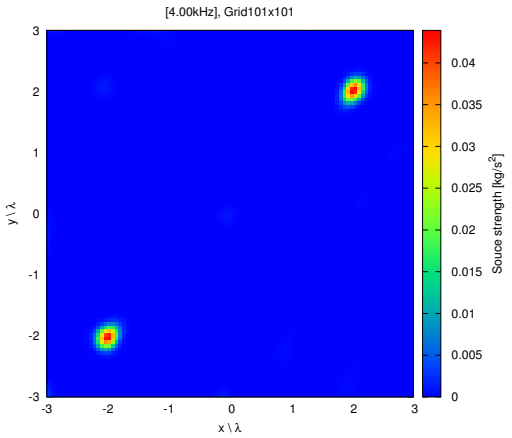

Figure 3: The reconstructed monopole source amplitude on the uniform source grid 101×101

density around the sources as in the 101×101 uniform grid. The source map spot size is about 0.3λ based on the spot half width. The spurious sources levels are higher than in the uniform model source distribution case. The integrated source amplitude is approximately $0.46[\mathrm{kg/s^2}]$ close to the values found on the uniform grid.

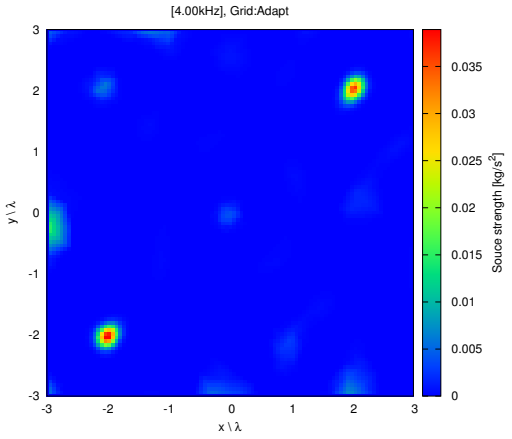

Figure 4: The reconstructed monopole sources on the adapted grid of approximately 2930 model sources. (The colour map is interpolated to a 101×101 grid)

The convergence of the IRLS iteration is plotted in Fig. 6. The plot shows the continuous decrease of the absolute value of solution summed for all grid points, that is the imposed constrain in the regularization method.

The effect of the non-uniform grid on the regularization method can be measured by comparing the

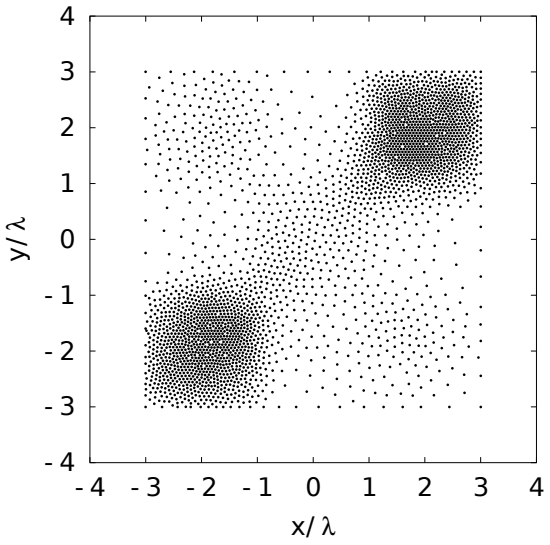

Figure 5: The adapted model source positions. $101x101$

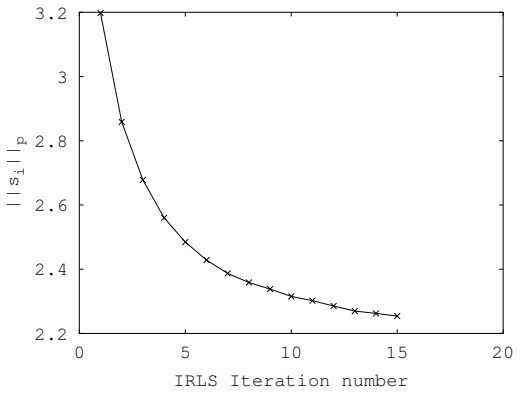

Figure 6: The convergence of the GIBF IRLS algorithm on the adapted grid.

singular value distribution of $\mathbf{V}$ (the spectrum of $\mathbf{V}$) in case of the uniform and the adapted grid [4]. The ratio of the highest and smallest singular values gives the condition number of the of the matrix. The value of the condition number indicates the level of ill-posedness of problem. The higher the condition number the more regularization should be used to overcome the amplification of the errors during the inversion process. The singular value distribution for the uniform grid and the adapted grid is shown in Fiq. 7.

The adaptation significantly changed the singular value distribution of $\mathbf{V}$. The singular values are significantly decreased. The condition number of the uniform grid model is 1225 while in the non-uniform grid model it is 1990. The adaptation of the grid is in-

creased the condition number, however this increase in not significant and it is not expected that it is changing the behavior of the inverse problem. The condition number of both cases can be considered as relatively small and the problem is not severely ill-posed.

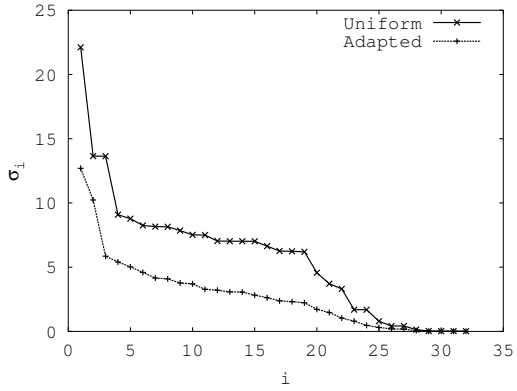

Figure 7: The distribution of the singular values of **V** for the two different meshes.

5. Discussion

Comparing the results obtained on the adapted and on the uniform grid both gives very similar source maps. The resolution and the source amplitudes are in good agreement. The uniform grid solution is a bit cleaner and the spurious sources are represented with smaller amplitude than in the case of the adapted grid solution. In this respect the uniform grid solution is slightly better than the non-uniform grid solution. The actual level of the spurious sources also depends on the used noise model. The applied random noise model significantly changed the distribution of the eigenmodes, that can be observed in Fig. 2. In case of the noiseless cross spectrum matrix only one non-zero eigenmode would exist. However in the present case all eigenmodes are non-zero and the second largest eigemode value is about 10% of the largest one. This implies the strong effect of the noise on the reconstruction and on the results. The test case shows that the algorithm handles well this level of random noise. The good resolution of the L_1 norm algorithm can be observed in both cases, that gives a resolution of approximately 0.3λ computed for the spot half width size on the source-map. This is very close to the $\lambda/4$ limit of the resolution. The usability of the L_1 norm generalized inverse beamforming method on arbitrary source map configuration is confirmed by the test, without the loss of the resolution or source amplitude prediction.

The convergence of the algorithm is good in the non-uniform grid also. The convergence characteristic shows that several additional iterations could be performed in order to further increase the accuracy. However it is not expected that the presented results changes significantly.

The inspection of the singular values draws an important behavior of the grid adaptation. The distribution of the singular values are significantly changed compared to the uniform grid, while the condition number, that is the ratio of the highest to smallest singular values, only slightly modified. Considering the fact that the number of model sources decreased by a factor of approximately 3.7 (from 10201 to approximately 2930) and their distribution changed to form two dense spots, suggest that the condition number cannot be significantly changed by varying the model source positions and number, in the same area, if the minimum distance between the points kept approximately unchanged. This is an interesting founding additionally to [8] where they found that the condition number is significantly affected by the microphone spacing, the source distances compared to the wavelength and the source array distance. They found also that the condition number of the problem is the smallest when the model source geometry is matching with the microphone array geometry (i.e. the distribution of the sources on the source plane are similar to the distribution of the microphones on the array plane). The fact that distributing the sources in an adaptive manner does not changed the condition number significantly, allows to prepare efficient adaptive grid techniques to resolve large source domains with the generalized beamforming method. These findings should be studied more precisely when efficient algorithms are intended to be created.

Concerning the required CPU time of the algorithm slightly better than linear speed-up have been found when considering the number of grid points used in the uniform and adapted grids. If the CPU time required for the uniform grid solution is denoted by T_u, then the solution of the same problem with the adaptive grid method is requires $\sim 0.27T_u$, from which the re-meshing is $\sim 0.04T_u$. The figures are measured on a 2.5Ghz Intel CPU with 6Mb cache and 2Gb of RAM. The numbers shows the required computational resource is reduced, and that can be still slightly improved by reducing the time required for the re-build of the source grid by using a faster implementation if the method of by using different technique. The used

method of [7] known to be a bit slow especially on large meshes.

The results emphasize that the appearance of the higher level of spurious sources depends on the model source grid. The distribution of the points has to be chosen carefully and low level of spurious sources can be achieved by using the uniform grid in the expense of higher computational cost. This results points out that the method to distribute the model source points is critical and can be the target of further improvements of the adaptive source grid beamforming technique.

6. Conclusion

In this paper the adaptive model source grid refinement technique is presented and evaluated with the help of a numerical test case. The generalized inverse beamforming method is used to retrieve the source positions and amplitudes with the L_1 norm formulation solved by the iteratively reweighed lest squares technique. For the regularization parameter choice the L-curve method is used. The retrieved source amplitudes and positions agree well with the imposed source parameters. The resolution is close to the $\lambda/4$ limit on the uniform as well as on the refined grid. The introduced significant level of random noise in the cross spectrum matrix of the microphone array does not prohibit the good quality reconstruction. On the other hand it causes the appearance of spurious sources on the source map especially in case of the adapted source grid. The level of these spurious sources can be possibly decreased with the careful choice of the grid size distribution function. This possibility has to be investigated when robust adaptation method is searched for.

The solution procedure with the mesh adaptation to the actual source geometry helped to reduce the CPU time of the computation with a factor of approximately 3.7. The reason is identified as the reduction of the model source points in the refined mesh. Roughly linear decrease of the computation time with the amount of source points in the final meshes can be achieved.

The condition number of the model problem is also investigated. It is observed that the condition number does not changed much between the uniform and refined mesh case. This is additionally supports the idea of using an adaptive model source distribution.

With the help of the adaptive model source grid technique the source domain size can be increased. Consequently one of the important source of error, the model error of the generalized inverse beamforming can be decreased. The grid adaptation algorithm therefore helps to extend the possibilities of the beamforming methodology for non-ideal acoustics environments.

Acknowledgments

This work is supported by the VALIANT project coordinated by the VKI.

References

[1] R. P. Dougherty, Noise source imaging by beamforming, in: Society of Automotive Engineers Brazil Noise and Vibration. Conference, Florianopolis SC, 2008.

[2] L. Koop, Beamforming methods in microphone array measurements theory, practice and limitations, in: M. L. Riethmuller, M. R. Lema (Eds.), Experimental Aeroacoustics, von Karman Institute, 2007.

[3] T. Suzuki, L1 generalized inverse beam-forming algorithm resolving coherent/incoherent, distributed and multipole sources, Journal of Sound and Vibration doi:10.1016/j.jsv.2011.05.021.

[4] P. C. Hansen, Rank-Deficient and Discrete Ill-Posed Problems, Society for Industrial and Applied Mathematics, 1998.

[5] P. C. Hansen, The L-Curve and its Use in the Numerical Treatment of Inverse Problems in Computational Inverse Problems in Electrocardiology, Advances in Computational Bioengineering, 2000.

[6] T. Suzuki, Generalized inverse beam-forming algorithm resolving coherent/incoherent, distributed and multipole sources, in: 14th AIAA/CEAS Aeroacoustics Conference (29th AIAA Aeroacoustics Conference), Vancouver, British Columbia Canada, 2008.

[7] P.-O. Persson, G. Strang, A simple mesh generator in matlab, SIAM Review 46 (2) (2004) 329–345.

[8] P. A. Nelson, S. H. Yoon, Estimation of acoustic source strength by inverse methods: Part i, conditioning of the inverse problem, Journal of Sound and Vibration 233 (4) (2000) 639–664. doi:10.1006/jsvi.1999.2837.

Prediction of Free and Scattered Acoustic Fields of Low-Speed Fans: Scattering of Tonal Fan Noise by a Rigid Corner

Korcan Kucukcoskun

École Centrale de Lyon, Laboratoire de Mécanique des Fluides et d'Acoustique, France, korcan.kucukcoskun@vki.ac.be

Supervisor: Christophe Schram

Associate Professor, Environmental and Applied Fluid Dynamics Department, von Karman Institute for Fluid Dynamics, Belgium, christophe.schram@vki.ac.be

University Supervisor: Michel Roger

Professor, Laboratoire de Mécanique des Fluides et d'Acoustique, École Centrale de Lyon, France, michel.roger@ec-lyon.fr.

Abstract

The exact analytical solution for the scattering of tonal fan noise by a rigid corner is addressed. The theory proposed for a monopole is first extended in order to compute the scattered field of a dipole. Combining the extended model with the dipole array approach, the scattered field of tonal fan noise by a corner is computed. Different blade forces and fan orientations are tested. A very good agreement is satisfied for all configurations in comparison with numerical simulations performed with a commercial BEM software.

Keywords: Aeroacoustics, tonal fan noise, scattering by a rigid corner.

1. Introduction

Exact analytical solutions addressing the acoustic free-field radiation from aerodynamic noise sources exist for many aeroacoustic problems. However, due to installation effects and presence of solid surfaces in radiation field, free-field propagation condition may become invalid. Scattering of acoustic waves by obstacles therefore needs being taken into account.

This paper deals with the analytical solution for the scattering of aerodynamic noise by a rigid corner and its application to tonal fan noise. One of the possible application areas is the cooling units of locomotives in parking position. The noise generated by a cooling unit located on the top of a locomotive and its scattered field by the corner of the locomotive-body may result in annoyance for passengers waiting on the platform. Noise generated by a small wind turbine located on the roof of a building and its effect on inhabitants can also be associated as another application area.

For low-frequency problems, numerical techniques such as Finite Element Method (FEM) and Boundary Element Method (BEM) are already in use to compute acoustic scattering by complex geometries [1]. However they are known to be dependent on the mesh resolution, such as the assumption of the requirement of 10 elements per wave length, λ [2; 3]. At higher frequencies, the number of elements required for an accurate prediction increases, hence the numerical solution becomes computationally demanding. Therefore, it is more convenient to use analytical solutions for high frequency problems if possible. For problems including simple geometries such as an infinite plane [4] or a semi-infinite plate [5], exact analytical scattering techniques can be used independent from the mesh resolution. An analytical method was proposed by MacDonald in order to deal with the acoustic scattering by a rigid wedge [6].

2. Scattering by a Rigid Corner

In the proposed analytical method, the scattering problem is treated as a boundary-value problem. A Green's function is derived for the Helmholtz equation with the exact boundary conditions. The rigid-wall boundary condition on the wedge surface and

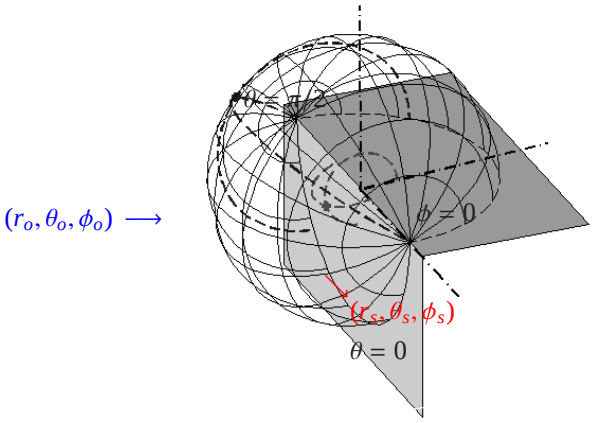

Figure 1: Sketch of the wedge, source-observer positions defined in polar coordinates

Sommerfeld radiation condition at large distances from the source are satisfied in the derivation.

MacDonald derived the Green's function for the Helmholtz equation around a wedge using polar coordinates [6]. The source and observer coordinates are (r_s, θ_s, ϕ_s) and (r_o, θ_o, ϕ_o), respectively shown in Figure 1. In MacDonald's formulation, the source is assumed to be located in the mid-plane of the rigid wedge, hence $\theta_s = \pi/2$.

For any wedge angle $0 < \phi < 2\pi$, the Green's function is defined as [6]

$$G(\mathbf{r}_s, \mathbf{r}_o) = \frac{2\pi}{\phi} \sum_{m=0}^{\infty} \varepsilon \cos(m'\phi_o)\ \cos(m'\phi_s) \sum_{k=0}^{\infty} 2^{m'}(2m' + 4k + 1) e^{(m'+2k+\frac{1}{2})\frac{1}{2}\pi \mathrm{i}} r_o^{-\frac{1}{2}} r_s^{-\frac{1}{2}} J_{m'+2k+\frac{1}{2}}(\kappa r_<) K_{m'+2k+\frac{1}{2}}(\mathrm{i}\kappa r_>) \cos(k\pi) \frac{\Pi(m' + k - 1/2)}{\Pi(k)\Pi(-1/2)} P^{-m'}_{m'+2k}(\cos\theta_o). \quad (1)$$

The parameter ε is 1 for $m = 0$ and 2 for $m > 1$ [7]. $P^{-m'}_{m'+2k}$ stands for the general Legendre function where $m' = m\pi/\phi$. J_υ and K_υ are the Bessel function of the first kind and of order υ and the modified Bessel function of order υ, respectively. Corresponding expressions with $r_>$ and $r_<$ interchange with the definition of the source and observer positions, $r_> = max(r_s, r_o)$ and $r_< = min(r_s, r_o)$. κ is equal to $2\pi/\lambda$.

Mel'nik and Podlipenko later proposed an expression for the scattering by a wedge containing soft walls for arbitrary source locations, as [8]

$$G(\mathbf{r}_s,\mathbf{r}_o) = \frac{\mathrm{i}\kappa}{\phi} \sum_{m=1}^{\infty} \sin(m'\phi_s)\ \sin(m'\phi_o) \sum_{n=0}^{\infty} (2n + 2m' + 1) j_{m'+n}(\kappa r_<) h^{(1)}_{m'+n}(\kappa r_>) \frac{\Gamma(n + 2m' + 1)}{\Gamma(n + 1)} P^{-m'}_{m'+n}(\cos\theta_s) P^{-m'}_{m'+n}(\cos\theta_o) \quad (2)$$

where j_υ and $h^{(1)}_\upsilon$ are the spherical Bessel and Hankel functions of the first kind and of order υ, respectively. The spherical functions are related to the cylindrical Bessel and Hankel functions via,

$$j_{m'+n}(\kappa r_<) = \sqrt{\frac{\pi}{2\kappa r_<}} J_{m'+n+1/2}(\kappa r_<) \quad (3)$$

$$h^{(1)}_{m'+n}(\kappa r_>) = \sqrt{\frac{\pi}{2\kappa r_>}} H^{(1)}_{m'+n+1/2}(\kappa r_>). \quad (4)$$

Combining formulations (1) and (2), the Green's function of a rigid wedge for arbitrary source and observer positions then becomes [14]

$$G(\mathbf{r}_s, \mathbf{r}_o) = \frac{-\pi\mathrm{i}}{4\phi\sqrt{r_s r_o}} \sum_{m=0}^{\infty} \varepsilon \cos(m'\phi_s) \cos(m'\phi_o) \sum_{k=0}^{\infty} (2m' + 4k + 1) \frac{\Gamma(2m' + 2k + 1)}{\Gamma(2k + 1)} P^{-m'}_{m'+2k}(\cos\theta_s) P^{-m'}_{m'+2k}(\cos\theta_o)\ J_{m'+2k+1/2}(\kappa r_<)\ H^{(1)}_{m'+2k+1/2}(\kappa r_>). \quad (5)$$

The trigonometric expansion of the Legendre function $P^{-m'}_{m'+k}(\cos\theta)$ employed in the computations [9] is

$$P^{-m'}_{m'+2k}(\cos\theta) = \frac{2^{1-m'}(\sin\theta)^{-m'}}{\sqrt{\pi}\Gamma(1/2 - m')} \sum_{n=0}^{\infty} \frac{\Gamma(n + 1/2 - m')\Gamma(2k + n + 1)}{\Gamma(n + 1)\Gamma(2k + n + m' + 3/2)} \sin[(2n + 1 + k)\theta]. \quad (6)$$

Formulation (5) is a general solution of acoustic diffraction by a wedge. Replacing the wedge angle ϕ by $3\pi/2$ results the specific case of a rigid corner. Equation (5) then becomes

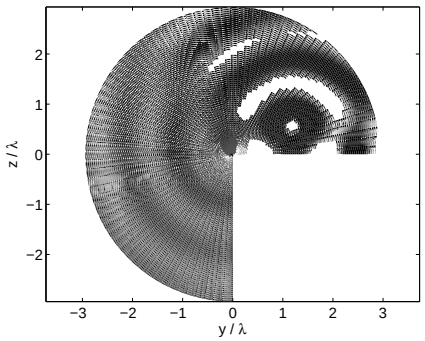

Figure 2: The map of acoustic potential of a point monopole nearby a rigid corner at $f = 10$ kHz. The point monopole is located at $(1.32\lambda, \pi/2, \pi/6.6)$.

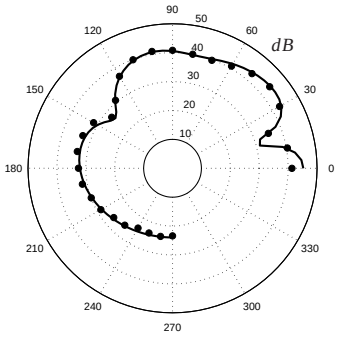

Figure 3: Directivity of a monopole located nearby of a rigid corner; analytical solution (line) and BEM results (symbols) at $f = 1$ kHz. The monopole is located at $(1.32\lambda, \pi/2, \pi/6.6)$ and observer distance is 3λ.

$$G(\mathbf{r}_s, \mathbf{r}_o) = \frac{-\mathrm{i}}{6\sqrt{r_s r_o}} \sum_{m=0}^{\infty} \varepsilon \cos(2m\phi_s/3)\cos(2m\phi_o/3)$$
$$\sum_{k=0}^{\infty} (4m/3 + 4k + 1) \frac{\Gamma(4m/3 + 2k + 1)}{\Gamma(2k+1)} P^{-2m/3}_{2m/3+2k}(\cos\theta_s)$$
$$P^{-2m/3}_{2m/3+2k}(\cos\theta_o)\, J_{2m/3+2k+1/2}(\kappa r_<)\, H^{(1)}_{2m/3+2k+1/2}(\kappa r_>). \tag{7}$$

Equation (7) is the exact solution for the acoustic waves scattered by a rigid corner. It will then be used to predict the scattered acoustic field of sources located in the vicinity of a rigid corner. For simplicity, a point monopole located nearby a corner will be investigated first. The theory will then be extended to a point dipole and finally it will be applied to a source representation of a fan.

2.1. Scattered field of a monopole

A first test is performed putting a point monopole at $(1.32\lambda, \pi/2, \pi/6.6)$ with respect to the origin of a rigid corner at $f = 10$ kHz. Figure 2 shows the map of the acoustic potential of a point monopole in the $\theta = \pi/2$ plane. Illuminated and shadow zones due to the corner can be seen clearly.

Once the Green's function is derived for a particular geometry, the acoustic field can then be computed for harmonic sources. The total acoustic field of a monopole is equal to

$$p(\omega, r) = G(\mathbf{r}_s, \mathbf{r}_o) q(\omega) \tag{8}$$

where $q(\omega)$ is the source strength of the point monopole.

A second test is performed in order to compare the analytical solution with numerical simulations. BEM is known to be able to handle scattered field problems for unbounded domains [3]. However, since at least 10 acoustical elements per wavelength is assumed to be required in an accurate BEM computation, in order to solve the BEM problem in a reasonable time, the tests are performed at lower frequencies. The computations are then performed at $f = 1$ kHz. A harmonic monopole source is located at $(1.32\lambda, \pi/2, \pi/6.6)$. The source strength of the monopole is selected as $q(\omega) = (0.01 + 0.01\mathrm{i}) kg/s^2$. In order to minimize effects of the free edges, a corner containing two $7\lambda \times 7\lambda$ flat plates is built. The size of the quadrilateral elements, $l \approx 0.1\lambda$, are satisfying the BEM criteria [2]. The total number of acoustic elements is then equal to 7200.

Figure 3 shows the directivity of the monopole-corner configuration at $f = 1$ kHz computed with the analytical solution (line) and with BEM (symbols). The radius of the field point mesh is selected as 3λ. The sound pressure levels are plotted in dBs. A very good agreement is observed in comparison of the amplitudes with the analytical and numerical solutions. The difference for all the directions is not more than 1 dB. It may be related to the scattering of the waves from the free edges of the acoustic mesh.

It appears that the scattered field of a point monopole by a rigid infinite corner can be computed accurately with the analytical model. Multipole monopoles can be summed up if needed. However, for a point dipole a specific development is more appropriate which is derived in the following section.

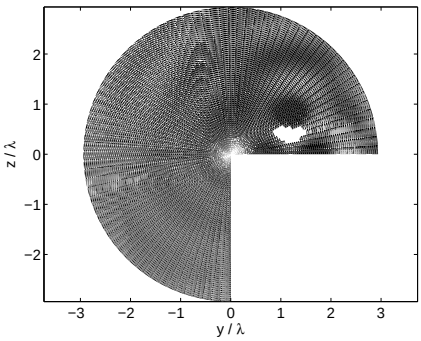

Figure 4: The map of acoustic potential of a point dipole nearby a rigid corner at $f = 10$ kHz. The point dipole is located at $(1.32\lambda, \pi/2, \pi/6.6)$.

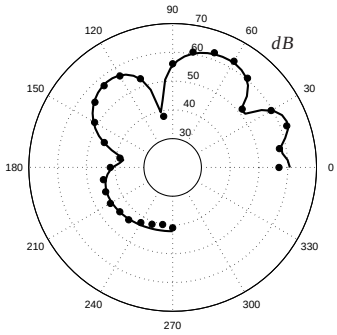

Figure 5: Directivity of a dipole located nearby a rigid corner; analytical solution (line) and BEM results (symbols) at $f = 1$ kHz. The dipole is located at $(1.32\lambda, \pi/2, \pi/6.6)$ perpendicular to $\phi = 0$ plane and observer distance is 3λ.

2.2. *Scattered field of a dipole*

The radiation field of a point dipole is related to the gradient of the Green's function with respect to the source coordinates. The acoustic pressure then becomes

$$p(\omega, r) = \nabla G(\mathbf{r}_s, \mathbf{r}_o) \cdot \mathbf{F}(\omega) \tag{9}$$

where $\mathbf{F}(\omega)$ is the source strength of the point dipole. Detailed derivations of the Green's function of a rigid corner for the dipole source can be found in the related reference [15].

A contour plot in the $\theta = \pi/2$ plane of the acoustic potential of a point dipole located nearby a corner is seen in Figure 4. The dipole is oriented at the same position as the monopole described in the previous section applying perpendicular to the $\phi = 0$ plane. The dipole-like behavior, reflected waves and shadow zone are clearly seen in the figure.

The analytical solution is again compared to the numerical model. A perpendicular dipole to $\phi = 0$ plane is again tested. The strength of the dipole is selected as $\mathbf{F}(\omega) = (0.01 + 0.01\mathrm{i})N$.

Figure 5 shows the directivity of the dipole-corner configurations at $f = 1$ kHz. The line and symbols represent the results obtained with the analytical solution and BEM model, respectively. A good agreement of the analytical and numerical solutions is again observed. The difference between the analytical and numerical results for a dipole is less than 1 dB.

Once validated for a single dipole, the theory is now extended to an equivalent distribution of a tonal fan noise source.

2.3. *Scattered field of tonal fan noise*

Several closed-form solutions addressing the free-field tonal fan noise exist in literature [11; 12; 13]. The exact closed-form analytical solution of free-field tonal fan noise is obtained by introducing the free-field Green's function into the solution of the inhomogeneous wave equation (see the related references [12; 13] for further derivation).

A tonal fan noise formulation taking near-field terms into account was derived by Roger [13]. The acoustic pressure at the nth harmonic of the blade passing frequency (BPF) at the observer is given as [13]

$$p'_{nB} = \frac{\mathrm{i}k_{nB}\Omega}{4\pi} \sum_{p=-\infty}^{\infty} \Big(-G^{(2)}_{nB-p} F^D_p x \sin\theta + G^{(3)}_{nB-p} F^R_p x \sin\theta + G^{(1)} (F^T_p (\zeta_3 - x\cos\theta) - F^{(R)}_p r') \Big) \tag{10}$$

for B equally spaced identical blades. F_R, F_D and F_T are the radial (R), drag (D) and thrust (T) forces acting

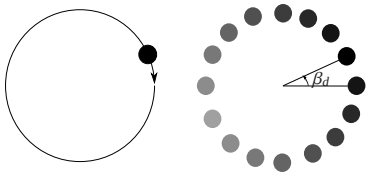

Figure 6: Equivalent fan source modeling strategies; (left) single rotating dipole, (right) continuous array of phase shifted dipoles.

on the blade, respectively. The applying forces are periodic with angular frequency Ω. $k_{nB} = nB\Omega/c_0$ is the wave number at the nBth harmonic. The geometrical parameters are shown in Figure 7.

Due to its periodicity, the sound field can be expanded as a Fourier series. G_m^N is the mth Fourier component of the auxiliary functions G_N (N=1,2,3). The auxiliary functions G_1, G_2 and G_3 are defined as

$$\begin{aligned} G_1(t) &= \frac{\mathrm{e}^{-\mathrm{i}k|\mathbf{R}|}}{|\mathbf{R}|^2}\left(1+\frac{1}{\mathrm{i}k|\mathbf{R}|}\right) \\ G_2(t) &= \sin(\Omega t+\varphi'-\varphi)\, G_1(t) \\ G_3(t) &= \cos(\Omega t+\varphi'-\varphi)\, G_1(t) \end{aligned} \tag{11}$$

with $k = \Omega/c_0$.

A common denominator of closed-form methods mentioned above is the consideration of a rotating dipole as shown in Figure 6 (left). However, introducing the gradient of the Green's function of a corner instead of the free-field one, it is not possible anymore to obtain an exact analytical solution for the scattered acoustic field of a fan operating next to a rigid corner. Still, an equivalent fan source can be obtained employing circular distribution of phase shifted dipoles as shown in Figure 6 (right). The phase difference of the dipoles is linked to the azimuthal position of the dipole, β_d. Using the dipole array, the equivalent free-field acoustic pressure of a B bladed fan at the nth harmonic of BPF then reads

$$p_{nB} = \frac{B}{N_d}\sum_{N_d} p_{nB,d} \tag{12}$$

where N_d is the number of dipoles in the azimuthal array.

Introducing Equation (9) into Equation (12), the total acoustic pressure field of the fan scattered by a rigid corner reads

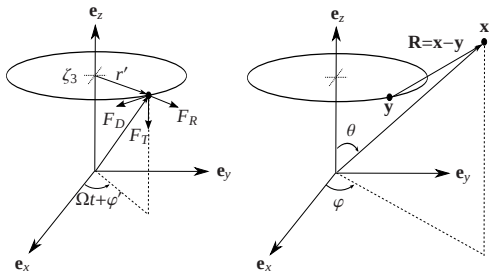

Figure 7: Source and listener coordinates

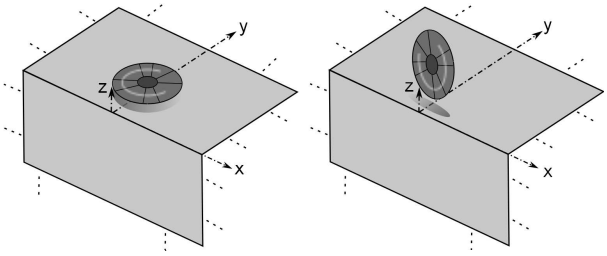

Figure 8: Sketches of fan-corner configurations; fans operating parallel to the *xy*-plane (left) and parallel to the *xz*-plane (right).

$$p_{nB}(\omega, r) = \frac{B}{N_d}\sum_{N_d} \nabla G(\mathbf{r}_s(\beta_d), \mathbf{r}_o)\cdot\mathbf{F}(\omega, \beta_d). \tag{13}$$

Since the Green's function of a rigid corner is extended for arbitrary positions of the source with respect to the wedge origin, it can now be used for any point dipole of the circular array. Equation (13) is a general solution for a fan operating out of a rigid corner. It can therefore be used for different fan-corner applications. The problem is first simplified to a fan operating parallel to the *xy*-plane. Figure 8 (left) shows the sketch of the simplified problem. A possible application area is the cooling units of locomotives in parking position as mentioned above. Only the scattering from the corner of the locomotive is addressed, neglecting other installation effects. Only one side of the locomotive is considered for the illustration.

The model fan employed has 10 equally spaced identical blades. The fan is rotating with 3000rpm making the blade loading frequency equal to $N/60$ = 50 Hz. Artificial blade forces are considered for the test case [15]. The blades are assumed acoustically compact and reduced to point dipoles. The radius of the fan source is selected as 0.15λ for the first BPF, f = 500 Hz. The center of the fan is located at $(0.6\lambda, \pi/2, \pi/12.8)$. The blade Mach number is then around 0.1, satisfying the low Mach number condition. The observers are located in the *yz*-plane with a radius of 1.5λ with respect to the origin of the corner.

Two low-speed axial fans are tested for comparison. The first test includes only the thrust force component, whereas the second one contains both drag and thrust force components as in a more realistic application. The radial forces are neglected for both configurations.

The problem is also dealt with the numerical approach combining Equation (10) with the BEM formulation. The same acoustic mesh and field points

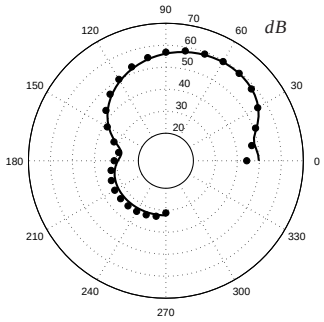

Figure 9: Directivity of a fan operating parallel to the *xy*-plane by a rigid corner; analytical solution (line) and BEM results (symbols) for test1. The fan center is located at $(0.6\lambda, \pi/2, \pi/12.8)$. Fan radius is 0.15λ. Observers are in the *yz*-plane at a radius of 1.5λ, at the first BPF, f = 500 Hz.

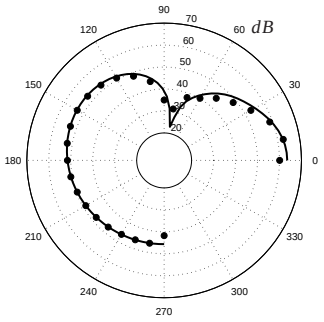

Figure 11: Directivity of a fan operating parallel to the *xz*-plane by a rigid corner; analytical solution (line) and BEM results (symbols) for test1. The fan center is located at $(0.66\lambda, \pi/2, \pi/6.6)$. Fan radius is 0.15λ. Observers are in the *yz*-plane at a radius of 1.5λ, at the first BPF, f = 500 Hz.

are used as in the dipole test case for the BEM model. The BEM problem is solved with LMS software Virtual Lab [3].

The scattered acoustic field directivities at the first BPF are seen for the first and the second tests in Figures 9 and 10, respectively. Line and symbols represent the analytical and numerical results, respectively. A good agreement is found between analytical and numerical solutions for both test fans. It is also seen that adding the drag component results higher acoustic pressure levels in the shadow zone.

A second fan orientation is selected where the rotation axis is perpendicular to the *xy*-plane, such as the example of small axial wind turbines located on the roof of buildings. A sketch of the problem is shown in Figure 8 (right). The problem can be dealt with the model described above only considering a new orientation of the fan. Same tests, one with only thrust and one with trust and drag forces, are selected for comparison. The rotation center is at $(0.66\lambda, \pi/2, \pi/6.6)$ and the fan is operating parallel to the *xz*-plane.

Figures 11 and 12 show the scattered-field directivities of the first and second tests, respectively. The line and symbols represent the analytical and BEM methods, respectively. It is seen that adding drag forces affects the acoustic field around the rotation plane. Finally, implementation of the proposed analytical model is validated against numerical simula-

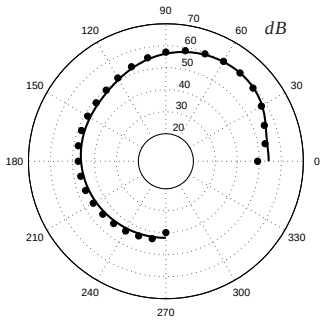

Figure 10: Directivity of a fan operating parallel to the *xy*-plane by a rigid corner; analytical solution (line) and BEM results (symbols) for test2. The fan center is located at $(0.6\lambda, \pi/2, \pi/12.8)$. Fan radius is 0.15λ. Observers are in the *yz*-plane at a radius of 1.5λ, at the first BPF, f = 500 Hz.

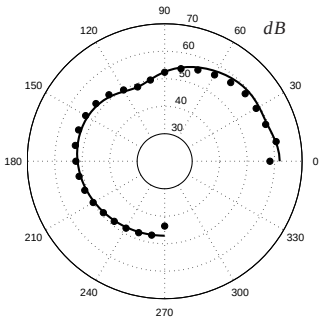

Figure 12: Directivity of a fan operating parallel to the *xz*-plane by a rigid corner; analytical solution (line) and BEM results (symbols) for test2. The fan center is located at $(0.66\lambda, \pi/2, \pi/6.6)$. Fan radius is 0.15λ. Observers are in the *yz*-plane at a radius of 1.5λ, at the first BPF, f = 500 Hz.

tions in all tested configurations.

As a result, extending the Green's function for arbitrary source positions and combining its gradient with the dipole array model, the scattered field of a low-speed axial fan by a rigid corner is computed accurately. For high frequency problems, where the numerical methods are demanding, the analytical solution can be useful irrespective of any mesh resolution issue.

3. Conclusion

The scattering of low-speed axial fan noise by a rigid corner is investigated numerically and analytically. It is seen that the scattered-field can be computed accurately with both numerical and analytical techniques. The numerical approach can be applied to more complex geometries for bounded and unbounded domains. On the other hand, for relatively simple configurations and where the numerical methods are computationally demanding, analytical solution can be useful independent from mesh resolution at any frequencies.

Acknowledgements

This work is supported by the FP7 Collaboration Project ECOQUEST (grant agreement no 233541).

References

[1] Desmet, W., Sas, P., "Introduction to numerical acoustics", In Lecture Notes of the ISAAC21 Course. K.U.Leuven, Leuven, Belgium, Sept. 23-24, 2010.

[2] Desmet, W., "Boundary element modeling for acoustics", In Lecture Notes of the ISAAC21 Course. K.U.Leuven, Leuven, Belgium, Sept. 23-24, 2010.

[3] Virtual Lab Rev 9: user manual, LMS International, 2009.

[4] Powell, A., "Aerodynamic noise and the plane boundary", J. Acoust. Soc. Am. 32 (8), 982:990, 1960.

[5] Ffowcs Williams, J., E., Hall, L., H., "Aerodynamic sound generation by turbulent flow in the vicinity of a scattering half plane", J. Fluid Mech. 40 (4), 657:670, 1970.

[6] Macdonald, H., M., "A class of diffraction problems", Proc. London Math. Soc. 14, 410:427, 1915.

[7] Pierce, A., "Acoustics: An introduction to its physical principles and applications", Ac. Soc. of America, 1989.

[8] Mel'nik, P., Podlipenko, Yu., K., "On Green's function for the Helmholtz equation in a wedge", Ukranian Mathematical Jou. 45 (9), 1471:1474, 1993.

[9] Abramowitz, M., Stegun, I., "Handbook of Mathematical Functions", Dover Publications, 1972.

[10] Crighton, D., G., Leppington, F., G., "On the scattering of aerodynamic noise", J. Fluid Mech. 46 (3), 577:597, 1971.

[11] Ffowcs Williams, J.E., Hawkins, D.L. "Sound generated by turbulence in arbitrary motion", Royal Society of London 264 (1151), 321:342, 1969.

[12] Goldstein, M.E. "Aeroacoustics", McGraw-Hill International Book Company, 1976.

[13] Roger, M., "Noise from moving surfaces", In advances in aeroacoustics and applications, VKI Lecture Series 2004-05, Rhode-St-Gense, 2004.

[14] Kucukcoskun, K., Roger, M., "On the scattering of aerodynamic noise by a rigid corner", AIAA paper, Accepted to the 18th AIAA/CEAS Aeroacoustics Conference, 2012.

[15] Kucukcoskun, K., "Prediction of free and scattered acoustic fields of low-speed fans", PhD Dissertation (in review), Ecole Centrale de Lyon, 2012.

Unsteady Panel Code for Airfoil Turbulence Interaction Computation

Leandro Dantas de Santana

Aeronautics and Aerospace Department, von Karman Institute for Fluid Dynamics, Belgium, leandro.santana@vki.ac.be

Supervisor: Christophe Schram

Associate Professor, Aeronautics and Aerospace Department, von Karman Institute for Fluid Dynamics, Belgium, christophe.schram@vki.ac.be

University Supervisor: Wim Desmet

Full Professor, KULeuven - Department of Mechanical Engineering, Belgium, wim.desmet@mech.kuleuven.be

Abstract

This paper describes the theoretical formulation of an unsteady panel code for the prediction of turbulence-airfoil interaction noise, valid for incompressible turbulent flows. This panel code formulation adopts the vorticity as elementary distributed singularity, in contrast with other approaches that use distributed sources and a constant intensity vortex sheet. Preliminary calculations present the quasi-steady and unsteady capabilities of this code to predict the response of a thin airfoil subjected to pitch oscillations and incoming vortical disturbances. The aerodynamic responses are compared with results obtained with the unsteady thin airfoil theory. The panel code is shown to predict with good accuracy unsteady response of an incompressible sinusoidal gust for reduced frequencies up to 8. This panel method advantages, from the traditional methods, for describing complex geometries with reasonable accuracy but very low computational cost, being attractive for conceptual design applications.

Keywords: unsteady panel code, incompressible turbulent flow, turbulence interaction noise, airfoil noise

1. Introduction

In turbofan engines and contra-rotating open rotors (CROR), airfoil-turbulence interaction typically considered as the main noise source generation mechanism. For an airfoil free of flow separation, the noise sources are mainly localized around the leading and trailing edges. The first is the main noise source when the incoming flow turbulence level exceeds a certain level. For lower levels of incoming turbulence, the scattering of self-generated boundary layer turbulence at the trailing edge dominates. The present work focuses on the incoming turbulence problem, relevant to the interaction between the wakes shed by the upstream rotor of a CROR and convected across the downstream rotor plane.

The problem has been already addressed by many authors since the seventies, and significant contributions to the field consist of semi-analytical approaches, mostly relying on thin-airfoil theory, based on a frequency-wavenumber representation of the incoming turbulence.[1; 2; 3; 4; 5] With the recent development of computational power, Large Eddy Simulation (LES) and Direct Numerical Simulation (DNS) techniques have been applied to obtain high accuracy flow descriptions [6; 7; 8] providing valuable input for prediction schemes based on the aeroacoustic analogy. These techniques have been proven to be powerful for simplified geometries, giving deep insight into complex physical phenomena. However, they still suffer from limited industrial applicability due to the large CPU effort involved in the flow calculation.

Discrete vortex boundary element methods are an interesting low-cost alternative to these expensive approaches, while offering more geometrical fidelity than the thin airfoil theories that linearize the airfoil shape as a flat plate with zero thickness, camber, and small angle of attack. The present work follows this alternative approach. Previous works in

this manner include Gennaretti et. al [9; 10] who proposed a unified boundary methodology for helicopter rotor aerodynamics and aeroacoustic predictions. Grace [11] discussed the respective merits of using time domain boundary element methods or harmonic gust analysis. Recently Glegg and Devenport [12] developed an unsteady vortex-based panel method and applied Amiet's theory to compute the far-field noise of turbulence-airfoil interaction. Their results are in good agreement with the flat plate analytical solution, nevertheless further comparison with experiments or high accuracy simulations of airfoils with realistic thickness, camber and angle of attack are still needed. Recently Zheng et al. [13] also used a discrete vortex method to predict the noise of a 3-elements high lift device. His panel method formulation, closer to the classical methods described by Cebeci et al. [14], shows a remarkable aerodynamic agreement with DNS simulations for the same geometry, with an angle of attack up to 8 degrees.

To reach its objective the present paper follows the Glegg and Devenport [12] unsteady vortex based panel method to predict the airfoil response to a turbulent inflow. In this paper, the aerodynamic unsteady response of this panel code is compared with analytical solutions obtained from the thin airfoil theory.

2. Panel method

Cebeci et al. [14] present a conventional two-dimensional panel method for the unsteady loading computation. This methodology is based on the Laplace's solution of a potential flow generated by the superposition of sources and vortex singularities, where the first is localized on each panel application point and the second is considered as a constant intensity sheet, placed along the airfoil chord. The system of equations is closed when the Kutta condition is applied to the trailing edge. The wake vortex sheet intensity is determined by Biot-Savart integration applied to the control surface in two dimensions. Conservation of the total circulation carried by the airfoil and wake is prescribed according to first principles.

While Cebeci's formulation has been extensively used in aeroelastic and wing morphing problems, it hasn't been as successful for aeroacoustic prediction. A more fruitful boundary element method for aeroacoustics, which applies the essence of the ideas described by Cebeci but with a different singularity distribution, has been presented by Glegg et. al [12]. In this approach the panel method adopts point vortices, instead of sources, as the base singularity. This singularity is distributed along each panel. This approach has been shown effective for predicting airfoil-turbulence interaction noise for reduced frequencies up to 10.

To describe the panel method used in this paper, the Howe [15] functional airfoil surface definition is adopted. In this formulation, for a given function f the region where $f(\boldsymbol{x}) = 0$ represents the body contour, $f(\boldsymbol{x}) < 0$ defines the airfoil interior region and $f(\boldsymbol{x}) > 0$ represents the exterior region. Using the Heaviside function $H(f(\boldsymbol{x}))$ it is possible to specify the non-penetration boundary condition to the velocity vector $\boldsymbol{v}$. Based on this definition, Howe proposes that the incompressible flow over a nonpermeable surface can be expressed as:

$$\begin{aligned}\nabla \times \nabla \times (H(f)\boldsymbol{v}) &= -\nabla^2 (H(f)\boldsymbol{v}) = \\ &= \nabla \times (H(f)\boldsymbol{\omega} + \boldsymbol{n} \times \boldsymbol{v}|\nabla f|\delta(f))\end{aligned} \tag{1}$$

with the following solution:

$$\begin{aligned}H(f)\boldsymbol{v}(\boldsymbol{x},t) = \nabla \times \int_D \frac{\boldsymbol{\omega}(\boldsymbol{y},t)}{4\pi|\boldsymbol{x}-\boldsymbol{y}|^3} dV(\boldsymbol{y}) + \\ + \nabla \times \int_S \frac{\boldsymbol{n} \times \boldsymbol{v}(\boldsymbol{y},t)}{4\pi|\boldsymbol{x}-\boldsymbol{y}|^3} dS(\boldsymbol{y})\end{aligned} \tag{2}$$

where D is the volume exterior to the airfoil surface S. The first term of Equation (2) represents the velocity induced by the wake vorticity computed by Biot-Savart integration. The second term of Equation (2) is the contribution of the bound vorticity to the airfoil surface velocity. Considering a right-handed coordinate system, where the indices 1, 2 and 3 represent the directions $\hat{i}$, $\hat{j}$ and $\hat{k}$, respectively, the induced velocity by a vortex of intensity $\gamma(\boldsymbol{y})$ is represented as:

$$\boldsymbol{n} \times \boldsymbol{v}(\boldsymbol{y},t) = -\gamma(\boldsymbol{y})\hat{k} \tag{3}$$

where $\boldsymbol{n}$ is the unit vector normal to the airfoil surface. Substituting Equation (3) in Equation (2) leads to:

$$\begin{aligned}H(f)\boldsymbol{v}(\boldsymbol{x},t) = \int_D \frac{\boldsymbol{\omega}(\boldsymbol{y},t) \times (\boldsymbol{x}-\boldsymbol{y})}{4\pi|\boldsymbol{x}-\boldsymbol{y}|^3} dV(\boldsymbol{y}) + \\ - \int_S \frac{\gamma(\boldsymbol{y})\hat{k} \times (\boldsymbol{x}-\boldsymbol{y})}{4\pi|\boldsymbol{x}-\boldsymbol{y}|^3} dS(\boldsymbol{y})\end{aligned} \tag{4}$$

Since we consider a two-dimensional problem, Equation (4) can be simplified to:

$$\begin{aligned}H(f)\boldsymbol{v}(\boldsymbol{x},t) = \int_C \int_{-\infty}^{\infty} \frac{\boldsymbol{\omega}(\boldsymbol{y},t) \times (\boldsymbol{x}-\boldsymbol{y})}{4\pi|\boldsymbol{x}-\boldsymbol{y}|^3} dy_3 dy_1 dy_2 + \\ - \oint_A \int_{-\infty}^{\infty} \frac{\gamma(\boldsymbol{y})\hat{k} \times (\boldsymbol{x}-\boldsymbol{y})}{4\pi|\boldsymbol{x}-\boldsymbol{y}|^3} dy_3 dS(\boldsymbol{y})\end{aligned} \tag{5}$$

where C represents the contour of the plane which contains the airfoil and its wake vorticity. Integrating in y_3 we obtain:

$$H(f)\boldsymbol{v}(\boldsymbol{x},t) = -\int_C \frac{\boldsymbol{\omega}(\boldsymbol{y},t)\times(\boldsymbol{x}-\boldsymbol{y})}{2\pi|\boldsymbol{x}-\boldsymbol{y}|^2}dy_1dy_2 + \\ + \oint_A \frac{\gamma(\boldsymbol{y})\hat{k}\times(\boldsymbol{x}-\boldsymbol{y})}{2\pi|\boldsymbol{x}-\boldsymbol{y}|^2}dS(\boldsymbol{y}). \quad (6)$$

Equation (6) can be solved numerically for the bound vortex sheet strength $\gamma(\boldsymbol{y})$ with the imposition of the non-penetration boundary condition on the airfoil surface control and the Kutta condition at the airfoil trailing edge. The time domain is discretized in interval Δt and the wake vorticity is represented by a sum of elementary vorticity elements as:

$$\boldsymbol{\omega}(\boldsymbol{y},t) = \sum_m \Gamma_m \hat{k}\delta(y_1 - y_1^{(m)}(t))\delta(y_2 - y_2^{(m)}(t)), \quad (7)$$

where Γ_m represents each discretized vortex circulation and $y^{(m)}$ its position on the coordinate reference system. Equation (6) then simplifies into:

$$H(f)\boldsymbol{v}(\boldsymbol{x},t) = -\sum_m \frac{\Gamma\hat{k}\times(\boldsymbol{x}-\boldsymbol{y}^{(n)}(t))}{2\pi|\boldsymbol{x}-\boldsymbol{y}^{(m)}(t)|^2} + \\ + \oint_A \frac{\gamma(\boldsymbol{y}\hat{k}\times(\boldsymbol{x}-\boldsymbol{y}))}{2\pi|\boldsymbol{x}-\boldsymbol{y}|^2}dS(\boldsymbol{y}) \quad (8)$$

which can be numerically solved by a time-marching routine and applying the Biot-Savart law.

Through Bernoulli equation, the instantaneous lift per unit span is determined at each time step:

$$L = -\oint_A p dx_1 = \frac{1}{2}\rho\oint_C |\boldsymbol{v}|^2 dx_1 + \rho\oint_A \frac{\partial\phi}{\partial t}dx_1 \quad (9)$$

with ϕ defined as the velocity potential. The lift can be calculated from the vortex sheet strength as:

$$L = \frac{1}{2}\rho\oint_C \gamma^2 dx_1 + \rho\frac{\partial}{\partial t}\oint_A\int_0^s \gamma(s')ds'dx_1 \quad (10)$$

with all integrals performed along the airfoil blade contour.

3. Panel code validation

3.1. Steady lift

The following step is the unsteady panel code validation considering its static response verification. In order to validate its inviscid steady solution the developed code is verified against the XFOIL solution. The NACA 0012 pressure distribution is compared against the reference solution in Figure 1, along the airfoil chord, for angles of attack of 0^o, 5^o and 10^o.

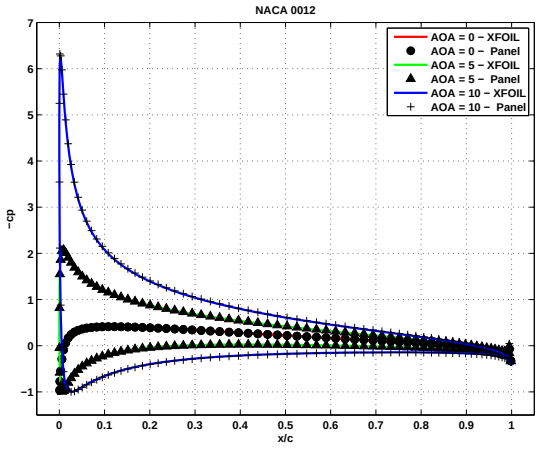

Figure 1: Steady cp comparison with XFOIL for the airfoils NACA 0001, NACA 0005, NACA 0012 and NACA 0024.

3.2. Unsteady response - The Wagner Function

Once the steady solution is verified, the next step is to compare the unsteady panel code response with a case with known analytical solution. A first verification case is the Wagner function. This solution is based on the linearized airfoil theory, valid for very thick airfoils subjected to small angles of attack. This function expresses the time domain airfoil lift, when subjected to an impulsive angle of attack variation. The impulsive change of the angle of attack generates a strong starting vortex, which by turns, influences the airfoil velocity. Immediately after the angle of attack impulse, the airfoil lift is considered as half of the steady lift. As the starting vortex is convected with the flow speed, its influence over the airfoil is reduced and, after enough time, its influence completely disappears and the flow becomes steady.

An approximation to the Wagner function is given by the equation:

$$\Psi(t) = 1 - \Phi_1 e^{-\epsilon_1 U_\infty t/b} - \Phi_2 e^{-\epsilon_2 U_\infty t/b} \quad (11)$$

where $\Phi_1 = 0.165$, $\Phi_2 = 0.335$, $\epsilon_1 = 0.0455$ and $\epsilon_2 = 0.3$, so that and the time domain lift coefficient is given by:

$$cl(t) = 2\pi\alpha\Psi(t) \quad (12)$$

and the lift force time variation becomes:

$$l(t) = \rho\pi U^2 c\alpha\Psi(t) = \rho\pi U c w\Psi(t) \quad (13)$$

where $w = U\alpha$ is the downwash velocity.

Figure 2 presents a comparison of the results obtained by the unsteady panel code and the airfoils NACA 0001, NACA 0005, NACA 0012 and NACA 0024. Here the airfoil NACA 0001 is considered as an airfoil which satisfies the thin airfoil theory due to its reduced thickness.

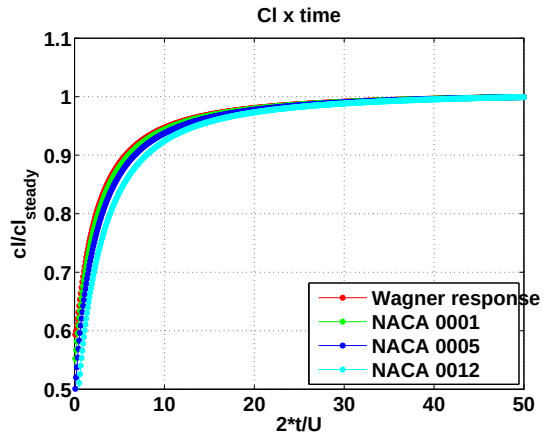

Figure 2: Airfoil lift response to an impulsive variation on angle of attack.

3.3. Unsteady response - The Sears Function

The Wagner function is an interesting first assessment of the unsteady panel code capabilities to predict the time domain unsteady lift, but, impulsive increases in angle of attack are not very common and generally speaking the the flow ingested by a lifting surface is not homogeneous, suffering variations of velocity module and angle of attack. In principal, these inhomogeneities can be decomposed by a series of trigonometric functions, which in turn can be representative as a sum of sinusoidal form gusts. A direct consequence of considering the airfoil impacting flow as an sum of sinusoidal gusts is that its time domain lift variation $F(t)$ can be directly represented in the frequency domain as $\tilde{F}(\omega)$.

In the Sears theory the flow inhomogeneities are considered to travel frozen along the airfoil chord, unaffected by its pressure field, which means that their decaying time is large, in comparison with the characteristic traveling time along the airfoil chord. Considering that the transverse disturbances are mostly responsible for the unsteady loads and considering that linearized airfoil theory is valid (the thickness, camber and angle of attack small) it is possible to affirm that the transverse gust component is predominant over the longitudinal one.

If steady inhomogeneous flow is assumed in a frame of reference moving with the flow, by means of a Fourier analysis of this flow, it can be decomposed into a series of transverse sinusoidal gusts, in the sense of unsteady aerodynamics, which can be characterized by the chord-wise wavenumber k_1 and its convection speed $U\infty$ as $\omega = k_1 U_\infty$. At a given value of ω or k_1 the Fourier coefficient $\tilde{F}(k_1)$ of the total unsteady lift force is determined by the Sears theory, in terms of transverse fluctuation amplitude $\tilde{w}(k_1)$. The connection between the lift and the upcoming gust is represented on Equation 14:

$$\tilde{F}(k_1) = \pi\rho c U\infty \tilde{w}(k_1)\bar{T} \tag{14}$$

where $\bar{T}$ is an additional aerodynamic transfer function.

In this way the local instantaneous lift fluctuation, per unit span, is given by:

$$l(k_1, y_1, t) = 2\rho_0 U_0 \tilde{w}(k_1) \sqrt{\frac{1-y_1^*}{1+y_1^*}} S^*(k_1^*) e^{-i\omega t} \tag{15}$$

where $y_1^* = 2y_1/c$ is the non-dimensional chord-wise coordinate, with reference to the mid chord, and $k_1^* = k_1 c/2$ is the non-dimensional aerodynamic wave number of the incident fluctuation, in the chord-wise direction. The theory applies to a given wavenumber and requires a Fourier analysis of the incident fluctuations. $S(k_1^*)$ is the known Sears function which is expressed in terms of Bessel functions as:

$$S(k_1^*) = \frac{2}{\pi k_1^*} \left([J_0(k_1^*) - Y_1(k_1^*)[- i\,[J_1(k_1^*) + Y_0(k_1^*)[\right)^{-1} \tag{16}$$

For the comparison of the developed code against the Sears function the airfoil NACA 0001 is considered as the flat plate, where the linearized airfoil theory is applicable. To assess the capabilities of the present code to compute the unsteady response of thicker airfoils to a sinusoidal type gust the NACA 0005, NACA 0012 and NACA 0024 are considered as well. The Figure 3 shows the panel's code obtained response compared with the analytical Sears function solution.

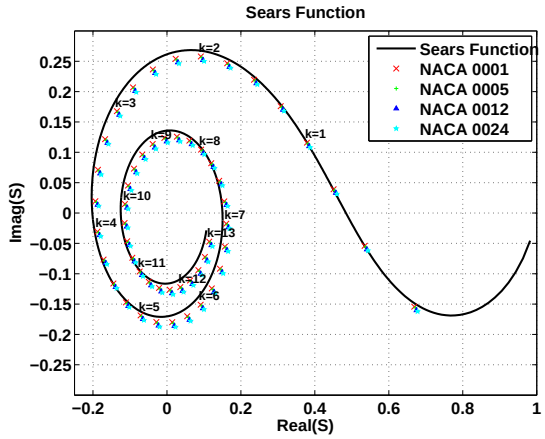

Figure 3: Airfoil lift response to a sinusoidal form impact gust.

4. Conclusions

This paper describes the aerodynamic part of validation of an unsteady panel code to be used for turbulence-airfoil interaction noise. This code is valid for incompressible flows and it is able to describe sinusoidal gusts with reduced frequency up to 8. The steady solution of this code perfectly matches with the results given by traditional panel codes. With regard to the unsteady solutions, for the case of an impulsive angle of attack variation, this code gives an overshoot of the lift for the initial time steps mainly, due to the intensity of the starting vortex, which influence is reduced as it is convected with the flow speed, and consequently the solution smoothly converges to the stationary one. The second unsteady testing case, where an sinusoidal gust impinges the airfoil surface it is seen that the thickness effects diverges the panel code solution from the analytical one. Based on this two unsteady analysis, it can be concluded that this unsteady panel code is suitable for airfoil surface forces prediction, which information is required for the turbulence-airfoil interaction noise prediction. Future works intend to present acoustic comparison against analytical solution cases, high precision simulations and experiments. The present results encourage further studies, because of the presently developed panel code presents very low computational cost when compared to traditional aeroacoustic codes, but shows potential to predict the airfoil with the reasonable precision necessary in conceptual design engineering applications.

5. Acknowledgments

Leandro D. Santana acknowledges the Brazilian Coordination for Improvement of Higher Education Personnel - CAPES - process number BEX-0520-10-1. The support of the European Commission, provided under the FP7 DINNO-CROR project (Grant Agreement no 255878), is gratefully acknowledged as well.

References

[1] R. Amiet, Acoustic radiation from an airfoil in a turbulent stream, Journal of Sound and Vibration 41 (4) (1975) 407 – 420. doi:10.1016/S0022-460X(75)80105-2.

[2] H. M. Atassi, The sears problem for a lifting airfoil revisited - new results, Journal of Fluid Mechanics 141 (1984) 109–122. doi:10.1017/S0022112084000768.

[3] H. M. Atassi, J. Grzedzinski, Unsteady disturbances of streaming motions around bodies, Journal of Fluid Mechanics 209 (1989) 385–403.

[4] M. Howe, Correlation of lift and thickness noise sources in vortex-airfoil interaction, Journal of Sound and Vibration 137 (1) (1990) 1 – 7. doi:10.1016/0022-460X(90)90713-A.

[5] M. R. Myers, E. J. Kerschen, Influence of incidence angle on sound generation by airfoils interacting with high-frequency gusts, Journal of Fluid Mechanics 292 (1995) 271–304. doi:10.1017/S0022112095001522.

[6] H. J. Kim, S. Lee, N. Fujisawa, Computation of unsteady flow and aerodynamic noise of naca0018 airfoil using large-eddy simulation, International Journal of Heat and Fluid Flow 27 (2006) 229–242.

[7] S. Moreau, J. Christophe, M. Roger, Les of the trailing-edge flow and noise of a naca0012 airfoil near stall, in: Center for Turbulence Research Proceedings of the Summer Program 2008, 2008.

[8] R. Sandberg, L. Jones, Direct numerical simulations of airfoil self-noise, Procedia Engineering 6 (2010) 274 – 282. doi:10.1016/j.proeng.2010.09.029.

[9] M. Gennaretti, L. Luceri, L. Morino, A unified boundary integral methodology for aerodynamics and aeroacoustics of rotors, Journal of Sound and Vibration 200 (4) (1997) 467 – 489. doi:10.1006/jsvi.1996.0713.

[10] M. Gennaretti, G. Bernardini, Novel boundary integral formulation for blade vortex interaction aerodynamics of helicopter rotors, AIAA Journal 45 (6) (2007) 1169–1176.

[11] S. M. Grace, Unsteady blade response: The bvi model vs. the gust model, in: 7th AIAA/CEAS Aeroacoustics Conference, 2001.

[12] S. A. Glegg, W. J. Devenport, Panel methods for airfoils in turbulent flow, Journal of Sound and Vibration 329 (18) (2010) 3709 – 3720. doi:10.1016/j.jsv.2010.03.007.

[13] Z. Zheng, B. Tan, Y. Xu, Near-field fluctuations and far-field noise of a three-element airfoil system by a discrete vortex method, Applied Mathematics and Computation 216 (4) (2010) 1072 – 1086. doi:DOI: 10.1016/j.amc.2010.01.129.

[14] T. Cebeci, M. Platzer, H. Chen, K.-C. Chang, J. P. Shao, Analysis of Low-Speed Unsteady Airfoil Flows, Horizons Publishing Inc., 2005.

[15] M. S. Howe, Acoustics of Fluid-Structure Interactions, Cambridge University Press, 1998.